

UV Diagnostics of Outflow Mechanisms in Five Radio-Quiet Obscured Quasars

ELISE KESLER,¹ SEAN D. JOHNSON,¹ JONATHAN STERN,² ZHUOQI LIU,¹ AND COLLABORATORS

¹*Department of Astronomy, The University of Michigan, 500 S State St, Ann Arbor, MI, 48109, USA*

²*School of Physics and Astronomy, Tel Aviv University, 69978 Tel Aviv, Israel*

ABSTRACT

Feedback from active galactic nuclei (AGN) is widely acknowledged as a primary process regulating the growth of massive galaxies, though the mechanisms driving this feedback are debated. Prevailing theories suggest that radio-quiet AGN feedback is driven by radiation pressure acting directly on the interstellar medium (ISM) via dust or by hot winds entraining the ISM, but the relative importance of these mechanisms is uncertain. Ratios of highly ionized UV emission lines serve as effective diagnostics of AGN feedback mechanisms due to their sensitivity to the density structure within ionized clouds. This study presents the first analysis of far-ultraviolet (FUV) spectra from five low-redshift galactic-scale outflows in obscured quasars using Hubble’s Cosmic Origins Spectrograph. By comparing narrow-line region UV emission line ratios to theoretical models with varying importance of the two driving mechanisms, we find three out of five targets fall within the radiation pressure-dominated regime. Another target falls between model predictions, but slightly favors the radiation pressure-dominated regime. The lowest luminosity object in our sample may have a dynamically important hot wind component, but non-detections prevent a clear conclusion in this case.

Keywords: Active galactic nuclei (16) — Quasars (1319) — Galactic winds (572) — Supermassive black holes (1663) – Active galaxies (17)

1. INTRODUCTION

By incorporating feedback from active galactic nuclei (AGN) as the primary regulator of massive galaxy evolution, many current large-scale cosmological models successfully reproduce key observable phenomena (see [Bessiere et al. 2024](#), and references therein). These include the well-established correlations between the properties of supermassive black holes (SMBH) and their host galaxies ([Cattaneo et al. 2009](#); [Kormendy & Ho 2013](#)), the suppression of star formation in massive galaxy halos ([Behroozi et al. 2013](#); [Su et al. 2021](#)), and the exponential break in the galaxy luminosity function ([Bower et al. 2006](#); [Weigel et al. 2017](#)).

The effectiveness of these models has positioned AGN feedback as a cornerstone of modern theories of massive galaxy evolution (for reviews, see [Harrison 2017](#); [Morganti 2017](#); [Martín-Navarro et al. 2018](#); [Laha et al. 2021](#)). However, the mechanisms driving this feedback remain enigmatic, especially for radio-quiet quasars that dominate AGN demographics, but which lack the dramatic radio jets that are observed driving feedback in rarer radio-loud systems (e.g. [Hardcastle & Croston 2020](#)).

Two primary theories propose that outflows from radio-quiet quasars result from: (1) direct radiation pressure on dust in the interstellar medium (ISM) or (2) ISM entrainment by a hot wind originating from the nucleus. Determining which of these is the primary driver is a subject of active research and debate (for a review, see [Singha et al. 2023](#)).

In the case of radiation pressure-driven winds, absorption and potentially scattering of photons in dusty gas surrounding an AGN create pressure, expelling surrounding material as an outflow ([Murray et al. 2005](#); [Ishibashi et al. 2018](#); [Arakawa et al. 2022](#)). Radiation pressure also compresses the outflowing gas into a stratified pressure gradient, creating a layered ionization structure with the most highly ionized species in the outermost layers closest to the AGN and lower ionization states in the interior of the clouds ([Dopita et al. 2002](#); [Baskin et al. 2013, 2014](#); [Stern et al. 2013, 2014](#); [Bianchi et al. 2019](#); [Netzer 2021](#)).

In hot wind-driven AGN outflow models, quasi-relativistic winds from the central supermassive black hole (SMBH) collide with the surrounding ISM and produce shocks that propagate in both directions on impact. These shocks produce a hot, volume-filling wind that can

contribute to observed outflows by entraining and accelerating the cooler ISM (King et al. (2011); Zubovas & King (2012); Faucher-Giguère & Quataert (2012)). The cool emission line gas is compressed by the confining hot gas pressure, so higher gas densities and a lower ionization parameter, U , are expected compared to outflows primarily driven by radiation pressure (Allen et al. 2008; Stern et al. 2016; Richings et al. 2021).

Recent surveys have largely characterized AGN outflows by tracing strong optical emission lines from low- and intermediate-ionization species, particularly [O III] (e.g., Greene et al. 2011; Harrison et al. 2014; Sun et al. 2017; Leung et al. 2019; Meena et al. 2021). While strong optical lines serve as sensitive tracers for identifying candidate AGN outflows, alone, they cannot effectively diagnose the mechanisms driving these outflows, as they lack sensitivity to the wide range of ionization states needed to distinguish between hot wind-driven and radiation pressure-driven outflows. As Stern et al. (2016) suggests, emission from highly ionized species offers more precise constraints on the contribution of hot winds in driving outflows.

Emission from highly ionized species is particularly useful because it is sensitive to differing density and pressure conditions of the gas (Stern et al. 2016). In radiation pressure-dominated outflows, the depth-dependent gas pressure and density produces emission lines across a broad range of ionization states. The predicted emission line ratios are highly precise with minimum dependence on model parameters, since in such outflows the ionization structure, thermal structure and density structure of the emission line gas are all set by the incident radiation (Stern et al. 2014, 2016; Bianchi et al. 2019). These precise predictions can be tested using UV to UV and UV to optical emission line ratios. Thus, constraining the importance of radiation pressure relative to a hot wind necessitates observation of species with a wide range of ionization levels. Combining UV emission lines such as O VI, N V, and C IV observable with sufficient sensitivity with the Hubble Space Telescope Cosmic Origins Spectrograph (*HST* COS; Green et al. 2012) with optical line observations is thus a particularly well-suited diagnostic tool.

In a pilot study aiming to constrain AGN feedback mechanisms with UV line emission, Somalwar et al. (2020) obtained the first spatially resolved UV spectra of a prototypical low- z obscured quasar, J1356+1026. Their *HST* COS G140L spectra revealed O VI/N V line ratios in both the narrow-line region and extended outflow consistent with models of AGN photoionized clouds driven primarily by radiation pressure. Building on this pilot study, we present circum-nuclear narrow-line region

UV emission spectra for a sample of five radio-quiet, low-redshift (z) obscured quasars exhibiting galactic-scale outflows. In order to use nuclear UV emission lines as diagnostics, we obtained *HST* COS observations in the FUV range of the circum-nuclear narrow-line region for all five of our targets. In Section 2, we discuss the target selection process, optical SDSS data, and FUV *HST* COS observations. Our resulting UV and optical emission line fluxes are discussed in Section 4. We compare observed UV to UV and UV to optical emission line ratios to theoretical models of these ratios as a function of the relative importance of hot gas and radiation pressure using models from Stern et al. (2016). We discuss these emission line ratios and their implications in Sections 4 and 5.

Throughout our analysis, we adopt a flat Λ cosmological model with values of $H_0 = 70$ km/s/Mpc, $\Omega_m = 0.3$, $\Omega_\Lambda = 0.7$.

2. OBSERVATIONS AND DATA REDUCTION

2.1. Target Selection

To gain insights into the relative importance of radiation pressure and hot winds for driving AGN feedback (see discussion in Section 1), we targeted a sample of five radio-quiet obscured quasars exhibiting galactic-scale outflows for COS observations of the O VI, N V, and C IV narrow-line region nuclear emission lines. These highly ionized lines serve as effective diagnostics of AGN feedback mechanisms due to their sensitivity to the density structure within ionized clouds (Stern et al. 2016).

Radio-quiet obscured quasars are ideal targets for our diagnostics. Dust in the obscured quasar hosts acts as a natural coronagraph, blocking the bright central nucleus and allowing observations of any extended outflows and conditions in the narrow-line region. Observing the O VI, N V, and C IV features within the COS FUV window requires redshifts between ≈ 0.1 and ≈ 0.17 . Therefore, we identified obscured quasars in this redshift range with evidence for galactic-scale, extended (≈ 10 kpc) outflows previously published in the literature by Greene et al. (2011), Harrison et al. (2014), and Sun et al. (2017). All three of these surveys identified candidate extended outflows from previous catalogs of Type 2 quasars (Reyes et al. 2008; Mullaney et al. 2013) from the Sloan Digital Sky Survey (SDSS; York et al. 2000) using optical [O III] emission lines as an outflow tracer and observed them with either long-slit or integral field optical spectroscopy. As a result of this selection, the candidate targets are fairly high luminosity systems, because luminous AGN are more likely to host outflows (Zakamska & Greene 2014; Polednikova, J. et al. 2015). All of our targets are

Table 1: Summary of *HST* COS observations.

Object	Grating	t_{exp} [s]	Start Date	Observation ID
J1356+1026	G140L	5200	2019-06-12	ldhv01010
J0841+0101	G140L	480	2020-02-26	le3i03010
J1000+1242	G140L	700	2020-05-26	le3i04010
J1222–0007	G140L	500	2020-05-18	le3i07010
	G130M	500	2020-05-18	le3i07010
J1255–0339	G130M	2300	2020-07-04	le3i08010
	G140L	2400	2020-07-04	le3i08020

potential or confirmed mergers, which is further discussed in Section 5.

First, we include *J1356+1026*, at $z = 0.123$, which was the subject of a pilot study using COS by Somalwar et al. (2020). It was chosen from Greene et al. (2011) based on their long-slit observations made using the Low-Dispersion Survey Spectrograph 3 (LDSS3, Allington-Smith et al. (1994)) at the Magellan/Clay telescope at the Las Campanas Observatory in Chile. J1356+1026 has the most pronounced extended and kinematically disturbed outflow out of their sample of 15 luminous, obscured, low- z quasars, and they estimate its [O III] emission radius as ≈ 10 kpc (also see Greene et al. 2012).

We selected two more targets from (Greene et al. (2011)): J1222–0007 and J0841+0101. *J1222–0007*, at $z=0.173$, is a spiral galaxy with an [O III] emission radius of ≈ 12.6 kpc and relatively high emission-line width (>500 km s $^{-1}$) (Greene et al. 2011). *J0841+0101*, at $z=0.111$, has a reported [O III] emission radius of ≈ 10 kpc (Greene et al. 2011).

We targeted *J1000+1242*, at $z=0.148$, based on the GMOS South IFU observations from Harrison et al. (2014). They selected it from the parent catalog of Mul-laney et al. (2013) as part of a representative study of type 2, low- z obscured quasars. They report an extended [O III]-emitting region radius of 4.3 ± 1.8 kpc.

We targeted *J1255–0339*, at $z=0.169$, based on the Magellan long-slit observations in Sun et al. (2017). It had the most extended narrow-line region in their sample of 12 nearby luminous obscured AGN, with a R_{NLR} (narrow-line region radius) of 33.5 ± 1.4 kpc.

2.2. SDSS Optical Data

To ensure a uniform analysis of the sample drawn from a number of AGN catalogs and produce the optical emission diagnostics discussed in Section 4, we performed our own emission line flux measurements of the nuclear optical spectra for the five targets from the SDSS DR17 Data Release (Abdurro’uf et al. 2022). We measured emission in [N II], H α , [O III], and H β . Prior to taking

flux measurements, we subtracted a linear continuum model, fit to line-free spectral regions near the emission lines. We performed the continuum fit and subtraction separately for the H α + [N II] and H β + [O III] regions.

Due to line blending, especially in the H α + [N II] region, we measured optical fluxes by fitting Gaussian profiles to each emission line. In most cases, the emission lines were blended or poorly described by a single Gaussian, so we used multiple Gaussian fitting models. We modeled both doublets ([N II] $\lambda\lambda 6550, 6585$ Å and [O III] $\lambda\lambda 4960, 5008$ Å) as double-peaked Gaussians with a fixed amplitude ratio of 2.95, the expectation given by the theory of atomic transitions Osterbrock & Ferland (2006).

Within the H α + [N II] region, we used three Gaussian components — one broad and two narrow — to fit all of the spectra except J0841+0101, which required only two components (one broad and one narrow). Since line width is expected to be consistent between the H α and [N II] emission lines of obscured quasars, we fixed each component to share values (ie., the broad H α and broad [N II] Gaussian components had the same line width).

Within the H β + [O III] spectral region, one broad and one narrow Gaussian effectively modeled the emission lines for J1000+1242, J0841+0101, and J1356+1026. An additional narrow component was needed for J1222–0007. In the case of J1255–0339, an additional narrow component was necessary to model the [O III] $\lambda\lambda 4960, 5008$ Å doublet, but adding a corresponding H β component did not improve the fit. Thus, we modeled it with three Gaussians fitting [O III] and two fitting H β . Again, similar components shared widths (ie., we modeled broad H β and broad [O III] with the same line width).

We applied a χ^2 minimization routine with the `lmfit` module (Newville et al. 2015) to find the best-fit model parameters for each region. Due to degeneracies between the line fluxes, widths, and redshifts of the individual Gaussian components, we evaluated the total flux posteriors using Markov Chain Monte Carlo (MCMC) methods from the `emcee` module (Foreman-Mackey et al. 2013) with walker start positions set around the best fit from the χ^2 minimization routine. The values and uncertainties reported in Table 2 are based on the total line flux posteriors marginalized over other parameters.

2.3. HST COS Observations and Data Reduction

To cover the wavelength range needed for UV emission-line diagnostics, we obtained far-ultraviolet (FUV) nuclear spectra for our five targets from the *HST* COS. The COS observations of J1356+1026 are from a pilot program (Somalwar et al. 2020, PID 15280). COS observations of the other four obscured quasars came from a

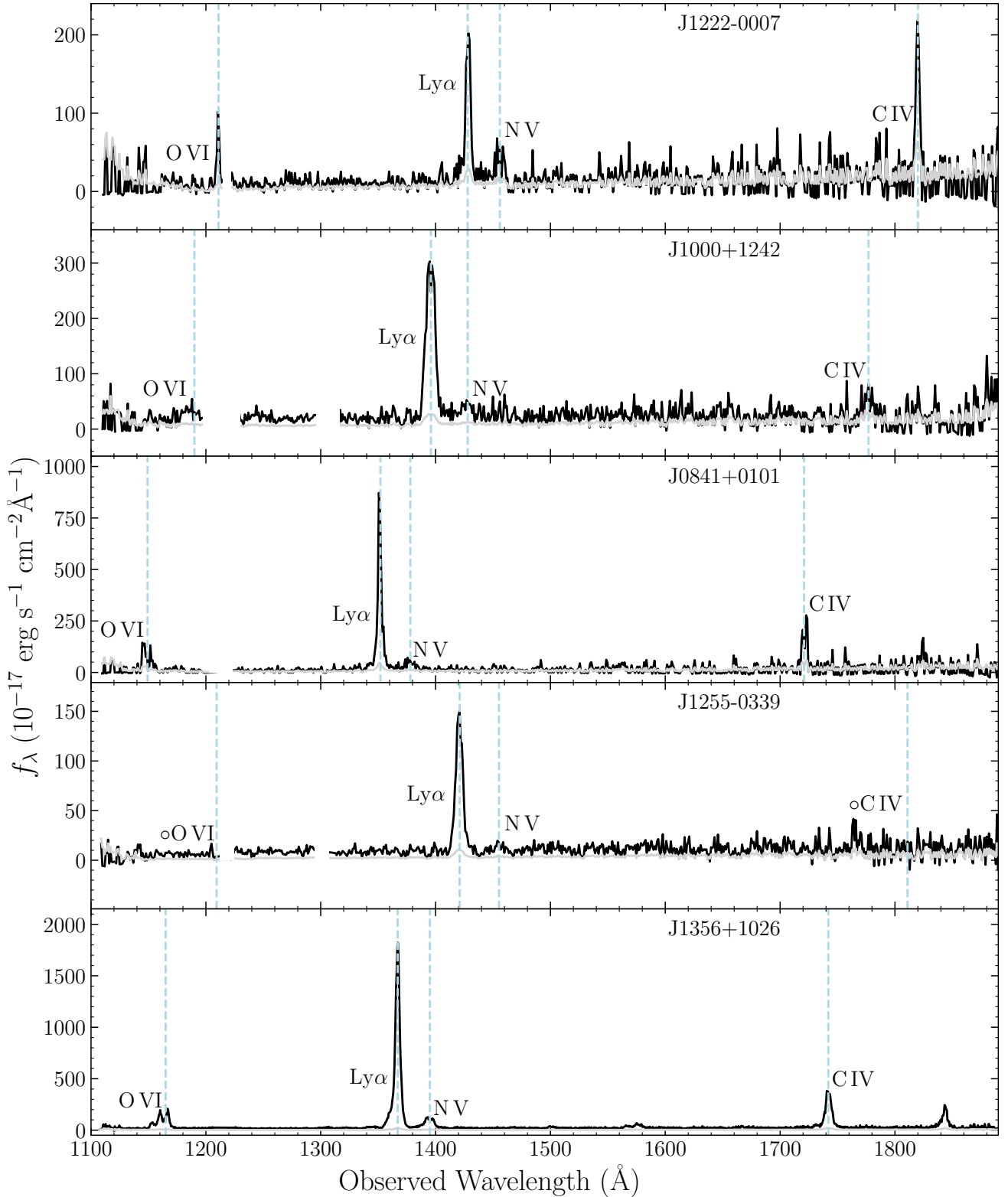


Figure 1: COS UV nuclear spectra for all five of our targets. Dashed light blue lines mark the expected location of the labeled spectral line given the target’s redshift. In the case of observed doublets (O VI $\lambda\lambda 1031, 1037\text{Å}$, N V $\lambda\lambda 1238, 1242\text{Å}$, and C IV $\lambda\lambda 1548, 1550\text{Å}$) the blue line is located at the midpoint of the expected location of each emission line. The two reported non-detections, O VI and C IV for J1255–0339, are denoted on their respective labels with open circles. To aid the visual inspection of emission lines, we have masked out the Ly α and O I geocoronal lines, where applicable, and set the y-axis limits so Ly α is similarly scaled for all five.

follow-up survey (PID 15935). All observations used for this analysis are summarized in Table 1.

The new *HST* COS observations were taken primarily with the G140L grating, but also supplemented with G130M in some cases. G140L has a relatively low resolution (resolving power ranging from 1,500-4,000) and was chosen for its wide wavelength range. Our G140L spectra cover wavelengths between ≈ 1100 -1900 Å. We used the higher-resolution G130M (resolving power ranging from 12,000-16,000) for two objects with O VI emission in close proximity to geocoronal H I Ly α emission (J1222-0007 and J1255-0339). The higher resolution of G130M enables better separation of the O VI line from geocoronal H I Ly α . We spliced the G130M spectra into the G140L spectra in the spectral region near O VI impacted by geocoronal emission for these two objects.

We retrieved the 1D spectrum associated with each exposure reduced using the CALCOS pipeline (Version 3.4.3; Kaiser et al. 2008) from the MAST archive. We then combined the individual exposures into final coadded spectra after masking out out pixels with data quality flags. In particular, we included only pixels with no anomalies or flagged only as in the detector shadow. We included pixels with detector shadow flags because the data reduction flat-fielding is sufficient to correct for the detector wire shadow so that any remaining artifacts are undetectable at our observed S/N (Soderblom et al. 2022). Our target spectra were taken with all four FP-POS positions. We co-added spectra onto a rebinned wavelength grid with a pixel scale of 1 Å for visualization purposes for all five of the targets.

In order to correct for the effects of Milky Way dust extinction, we used the extinction curve from Fitzpatrick (1999) implemented in the Extinction package (Barbary 2021) and A_V values estimated in the direction of each obscured quasar from the extinction map in Schlafly & Finkbeiner (2011). The resulting coadded and extinction-corrected spectra are shown in Figure 1. Within these spectra, we observe emission in the O VI $\lambda\lambda 1031, 1037$ Å doublet; the N V $\lambda\lambda 1238, 1242$ Å doublet; and the C IV $\lambda\lambda 1548, 1550$ Å doublet. The process we used to measure these emission line fluxes is described in Section 2.4, and the results are reported in Section 4.

2.4. UV Flux Measurements

Since the O VI, N V, and C IV UV emission lines are generally not blended with strong lines from other species, we measured their fluxes by applying direct Simpson integration to each individual emission line after subtracting a linear continuum fitted to nearby line-free spectral

regions. We do not treat individual doublet lines separately; i.e. the reported doublet emission flux values are the sum of both lines. During the integration process, we estimated flux errors from Poisson counting statistics. To verify the accuracy of these estimates, we also calculated the mean flux per pixel from surrounding line-free continuum areas for each individual line and determined its standard deviation. The consistency between these methods led us to adopt the Poisson error estimates which are reported here. We adopt a 3σ detection threshold, and report corresponding upper limits in the cases of non-detections.

The close proximity of the $\lambda\lambda 1031, 1037$ Å doublet to geocoronal Ly α resulted in partial blending in the cases of J1222-0007 and J1255+0339, despite the use of G130M data. To determine the extent of blending for J1222-0007, we compared the FWHM of the other measured doublets (N V $\lambda\lambda 1238, 1242$ Å and C IV $\lambda\lambda 1548, 1550$ Å) to the expected doublet separation. We found that the emission blue of geocoronal Ly α at the expected location of O VI had the smallest FWHM despite having the largest expected doublet separation. This indicates that the observed O VI emission line blue of geocoronal Ly α was the 1031 emission line, and the 1037 emission line was blended with geocoronal Ly α . To verify this and further examine the extent of the blending, we fit two Gaussians — one to each emission line in the doublet, with a shared emission line width — to the N V $\lambda\lambda 1238, 1242$ Å and C IV $\lambda\lambda 1548, 1550$ Å doublets and used the velocity dispersions from those fits as an initial guess in a fit of O VI $\lambda\lambda 1031, 1037$ Å, along with an additional Gaussian fit to geocoronal Ly α . Fixing the O VI doublet Gaussian widths to the N V velocity dispersion resulted in a good fit, supporting our hypothesis that the 1037 line was blended with geocoronal Ly α .

Given these results, we estimated the total O VI flux for J1222-0007 by considering the theoretical expectation for ratios between the O VI 1031 and 1037 emission lines. In the optically thin limit, the 1031 emission line is expected to be approximately twice as strong as the 1037 line, but in the optically thick limit there is an approximately 1:1 ratio (Draine 2011). Blending of the 1037 line with geocoronal H I Ly α prevents measurements of the line ratio, but the theoretical minimum and maximum line ratio enables us to place a robust constraint on the total O VI flux from the 1031 line alone. In particular, we report the measured total O VI flux as 1.75 times the 1031 flux measurement with an associated systematic uncertainty of 0.25 times the 1031 flux measurement.

Proximity of O VI to geocoronal Ly α also introduced additional uncertainty in the case of J1000+1242. Though a similar FWHM comparison to the one de-

Table 2: UV and optical nuclear emission line fluxes.

	Line	Flux (10^{-15} erg cm $^{-2}$ s $^{-1}$)	Centroid (Å)	SNR
J1356+1026	H I Ly α	94 ± 0.4	1365	240.0
	N V 1238.82/1242.80	9.5 ± 0.1	1394	94.5
	O VI 1031.92/1037.61	17 ± 0.2	1162	88.7
	C IV 1548.19/1550.77	26 ± 0.4	1740	58.4
	[O III] 4960/5008	167 ± 0.6		
	H β	18 ± 0.2		
	[N II] 6550/6585	27 ± 0.3		
	H α	63 ± 0.5		
J0841+0101	H I Ly α	34 ± 1.2	1350	29.6
	N V 1238.82/1242.80	3.8 ± 0.4	1378	11.6
	O VI 1031.92/1037.61	8.6 ± 0.9	1149	11.3
	C IV 1548.19/1550.77	11 ± 1.0	1720	7.3
	[O III] 4960/5008	100 ± 0.5		
	H β	8.5 ± 0.1		
	[N II] 6550/6585	12 ± 0.1		
	H α	35 ± 0.2		
J1000+1242	H I Ly α	27 ± 0.9	1396	32.2
	N V 1238.82/1242.80	2.5 ± 0.2	1424	13.4
	O VI 1031.92/1037.61 ^a	5.2 ± 0.3	1188	19.5
	C IV 1548.19/1550.77	7.3 ± 0.8	1779	7.7
	[O III] 4960/5008	119 ± 1.5		
	H β	9.0 ± 0.1		
	[N II] 6550/6585	32 ± 2.0		
	H α	51 ± 2.0		
J1222-0007	H I Ly α	10 ± 0.7	1426	15.9
	N V 1238.82/1242.80	3.2 ± 0.4	1455	9.2
	O VI 1031.92/1037.61	4.66 ± 0.94	1213	9.7
	C IV 1548.19/1550.77	8.9 ± 1.4	1817	6.0
	[O III] 4960/5008	109 ± 0.3		
	H β	11 ± 0.1		
	[N II] 6550/6585	19 ± 0.2		
	H α	45 ± 0.3		
J1255-0339	H I Ly α	11 ± 0.3	1421	37.0
	N V 1238.82/1242.80	0.9 ± 0.05	1450	45.0
	O VI 1031.92/1037.61 ^b	<0.9	1209	7.5
	C IV 1548.19/1550.77 ^b	<3.7	1811	—
	[O III] 4960/5008	10 ± 0.1		
	H β	2.4 ± 0.1		
	[N II] 6550/6585	9.7 ± 0.2		
	H α	14 ± 0.2		

^a Measurement based only on the 1031 line is visible for this object with total flux and error estimate reflecting allowed doublet ratios as described in Section 2.4.

^b Upper-limit flux estimated as the three sigma limit from Gaussian fits or direct integration as described Section 2.4)

scribed at the beginning of this section showed the O VI doublet to be distinctive from geocoronal Ly α , it was difficult to define the linear continuum and define the integration boundaries. The generally broad line profiles for J1000+1242 introduce additional uncertainty in the line flux due to choices of integration boundaries. To account for this added uncertainty, we adjusted the bounds repeatedly across the range of reasonable limits, and found flux differences of $\pm \approx 10\%$. We include this additional systematic uncertainty in our reported measurements and interpretation in this case.

Our two non-detections, C IV and O VI in the spectrum of J1255+0339, are reported here as upper-limits on the possible flux. We estimated an upper-limit flux for C IV by calculating the average flux per count multiplied by the gross counts within 23 Å of the expected line position. The choice of 23 Å for the integration limit when setting the flux upper limit is motivated by the width of this object’s Ly α emission line. This method was not useful for estimating the O VI upper-limit flux, since the area surrounding the expected line location included geocoronal Ly α . Thus, we estimated O VI as the three-sigma limit from a double Gaussian fit with the redshift fixed to the value measured in the SDSS spectrum of the AGN and the velocity dispersion fixed to that of Ly α for the same object.

3. AGN PHOTOIONIZATION MODELS

We compare our measured line ratios to two types of AGN photoionization models, calculated with CLOUDY (Ferland et al. 2017): (1) the more commonly used ‘constant density’ models, which assume the photoionized gas has some uniform density; and (2) hydrostatic models (e.g., Dopita et al. 2002; Groves et al. 2004; Stern et al. 2014, 2016) which assume the ionized gas achieves hydrostatic equilibrium with pressure sources including thermal pressure from a hot, volume-filling medium and radiation pressure due to emission from the quasar. Following Stern et al. (2016), we characterize these latter models by the ratio $P_{\text{hot}}/P_{\text{rad}}$, where P_{hot} is the thermal or ram pressure of a hot gas compressing the emission line cloud, and $P_{\text{rad}} \equiv L/(4\pi r^2 c)$ is the radiation pressure of the incident AGN radiation. In models where P_{hot} dominates, the gas pressure is effectively uniform and equal to P_{hot} throughout the cloud, so the ionized region where $T \sim 10^4$ K is effectively a constant density model. In models where P_{rad} dominates, gas pressure builds up within the ionized region as radiation pressure is absorbed, starting at P_{hot} at the exposed surface and reaching $\approx P_{\text{rad}}$ at the H I front (see Stern et al. 2016; Somalwar et al. 2020). In the limit $P_{\text{rad}} \gg P_{\text{hot}}$, predicted line ratios are independent of $P_{\text{rad}}/P_{\text{hot}}$. Assuming hy-

drostatic equilibrium in the emission line gas is plausible since the sound-crossing time is a few thousand years, compared to outflow evolution times of Myr or more (see Dopita et al. 2002; Namekata et al. 2014).

Other parameters are set to the following fiducial values, and are common between the two types of models. We assume a cloud that is optically thick to hydrogen ionizing photons at a distance of $r = 1$ kpc from the AGN, with an AGN luminosity of $L = 10^{46}$ erg s $^{-1}$ and ionizing spectral slope $\alpha_{\text{ion}} = -1.6$ ($L_\nu \propto \nu^{\alpha_{\text{ion}}}$ at wavelengths 6.2 – 1100 Å). The spectral shape in non-ionizing frequencies follows Laor & Draine (1993), though its effect on the predicted lines is minor. We use the standard Milky-Way ISM grain model implemented in CLOUDY with a graphite and silicate mixture and an MRN size distribution (Mathis et al. 1977), and metal abundances from Groves et al. (2006) including depletion onto dust grains and non-linear scaling of Nitrogen with metal mass Z (non-depleted abundances are consistent with ?). Our fiducial models assume twice the metal mass fraction and dust-to-gas mass ratio, \mathcal{D} , relative to Milky-Way ISM values, as observed in the centers of massive galaxies which are characteristic of AGN hosts (Kewley et al. 2006; Groves et al. 2006). To assess the sensitivity of our results to these ‘nuisance’ parameters, we run a grid of models with $-1.8 < \alpha_{\text{ion}} < -1.4$, $100 \text{ pc} < r < 10 \text{ kpc}$, and Z, \mathcal{D} between one and four times the Milky-Way ISM value. We demonstrate below that the choice of these parameters has far less an effect on the predicted line ratios than the assumed $P_{\text{rad}}/P_{\text{hot}}$ in the hydrostatic models or the assumed ionization parameter $U \propto L/(n_{\text{H}} r^2)$ in the constant density models.

4. RESULTS

To confirm the AGN nature of our objects and contextualize them within the general AGN population, we produced a BPT diagram (Figure 2, left panel) with diagnostic boundaries from Kewley et al. (2006), separating AGN from star-forming galaxies on a plot of $[\text{N II}]/\text{H}\alpha$ vs $[\text{O II}]/\text{H}\beta$. The BPT diagram confirms that all five targets fall within the expected range for Type 2 AGN. Also included on this plot are ratios given by the radiation pressure-dominated hydrostatic photoionized models. Four out of five targets fall within the RPC predictions, but one object (J1255–0339) has a lower $\log([\text{O III}]/\text{H}\beta)$ ratio than radiation pressure model expectations. In the right panel of Figure 2, we plot the total $[\text{O III}] \lambda\lambda 4960, 5007$ Å line luminosities versus redshifts for our sample, alongside data from the obscured quasar catalog in Reyes et al. (2008).

The UV spectra exhibit notable variations in line strengths across the sample. To provide context, we

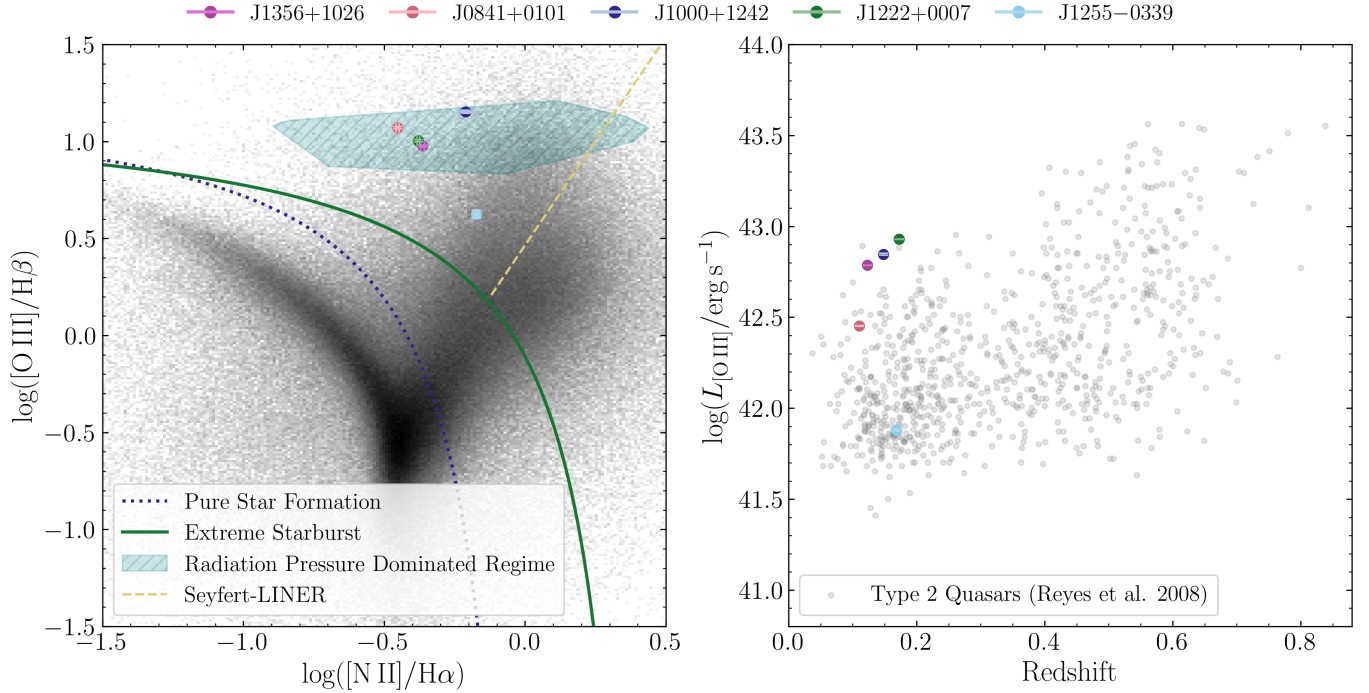


Figure 2: *Left panel:* BPT diagram confirming identification of objects as AGN, with target obscured quasars in purple and SDSS galaxies in greyscale for comparison (Abdurro’uf et al. (2022), Brinchmann et al. (2004), Kauffmann et al. (2003), Salim et al. (2007), Tremonti et al. (2004)). The solid green and dotted blue lines are the extreme starburst and pure star formation classification lines from Kewley et al. (2006). The Seyfert-LINER line from Kauffmann et al. (2003) is in orange. Error estimates for both axes are plotted in light purple. The range allowed by the Radiation Pressure Confinement (RPC) models ($P_{\text{rad}} \gg P_{\text{hot}}$) discussed in Section 3 is shown as a blue hatched region. *Right panel:* $[O\ III]$ luminosities measured from SDSS spectra vs redshift for our five targets plotted against those of the Type 2 Quasars catalog presented in Reyes et al. (2008). The 68% confidence interval errors for the $[O\ III]$ luminosities, plotted in another shade of purple, are smaller than the data points.

qualitatively compare the spectral line profiles of our targets to those of J1356+1026, which was previously examined in Somalwar et al. (2020). The line ratios in J0841+0101 and J1000+1242 closely resemble those of J1356+1026, although J1000+1242 displays noticeably broader spectral features. J1222-0007 exhibits a relatively high C IV to $\text{Ly}\alpha$ flux ratio compared to the other targets. J1255-0339, in contrast, shows weak UV emission in general, with non-detections of C IV and O VI. We provide upper-limit flux estimates for these undetected emission lines based on its expected the expected location and line widths inferred from detected UV lines (see Section 2.4 for details on this estimation). Table 2 summarizes the optical and UV line fluxes for all five targets, along with counts and signal-to-noise ratios for the UV lines only. Diagnostic ratios between the UV lines are shown and discussed in Section 5.

5. DISCUSSION

In Figures 3 and 4, we compare our measured optical and UV emission line ratios of $[O\ III]$, O VI, C IV, and N V to the models described in Section 3.

In the left panel of 3, the observed O VI/N V and O VI/C IV line ratios are relatively consistent with radiation pressure-dominated models ($P_{\text{hot}} \ll P_{\text{rad}}$) for four out of five of our targets (J1356+1026, J0841+0101, J1222-0007, and J1000+1242). Three of the four objects near the radiation-pressure dominated limit fall within the predicted model line ratio ranges of O VI/N V and O VI/C IV. J1222-0007 exhibits a slightly lower O VI/C IV line ratio than the radiation pressure-dominated models predict.

In the right panel of Figure 3, the observed O VI/ $[O\ III]$ for J1356+1026 and J0841+0101 fall within the radiation pressure-dominated range. Two other targets (J1222-0007 and J1000+1242) exhibit slightly lower O VI/ $[O\ III]$ ratios than the radiation pressure-dominated models predict. The inclusion of the $[O\ III]$ forbidden line ratio is

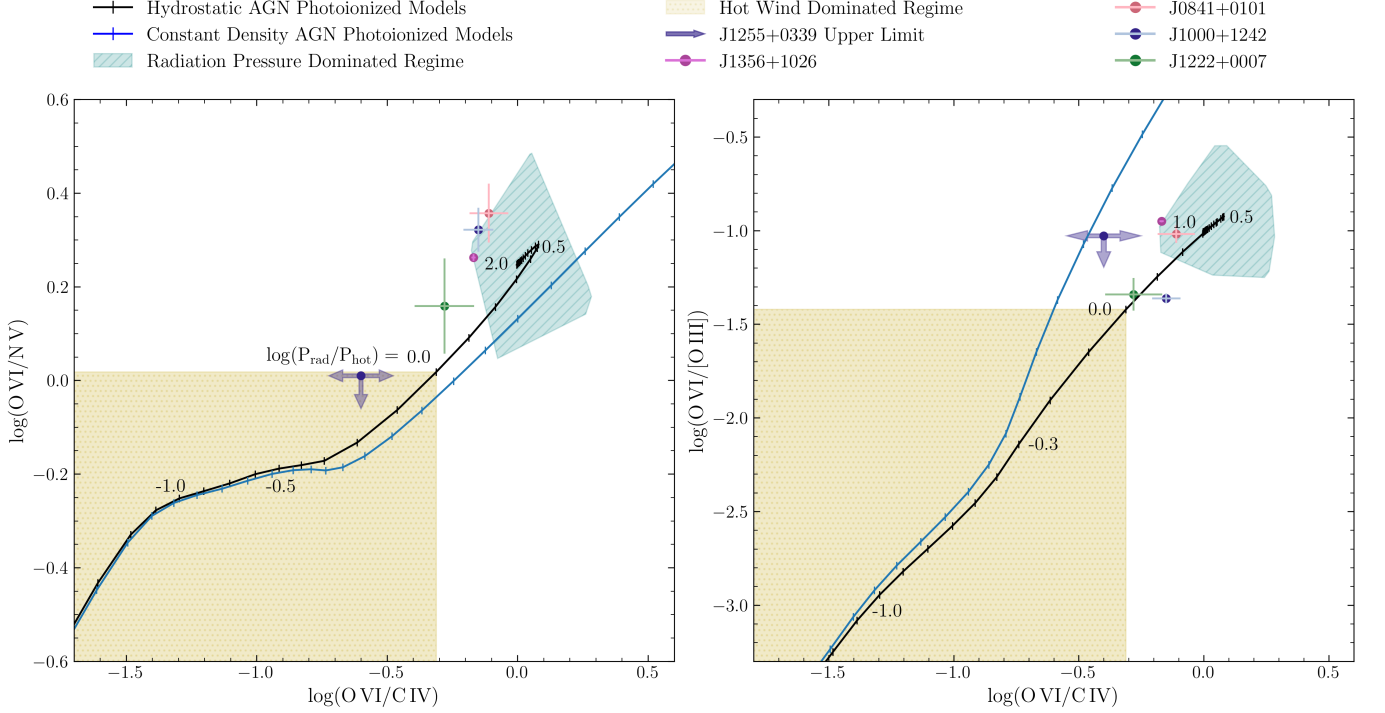


Figure 3: UV diagnostic line ratio diagrams for the archival sample of five obscured quasars with constraints on these transitions. In both panels, the observed line ratios and errors are shown as colored points. The upper-limit flux estimates for the J1255–0339 non-detections of O VI and C IV are shown as dark blue points with arrows indicating the estimated possible values. Models of AGN photoionized gas varying $P_{\text{hot}}/P_{\text{rad}}$ from Stern et al. (2016) ($Z/Z_{\text{sun}} = 2Z_{\text{sun}}$) are shown in solid black, with ticks marking steps of 0.1 dex in $P_{\text{hot}}/P_{\text{rad}}$. We represent the estimated radiation pressure-dominated regime by the teal, shaded region covered by $P_{\text{rad}} \gg P_{\text{hot}}$ models with parameters ranging from $1 < Z/Z_{\text{sun}} < 4$, $-1.8 < \alpha_{\text{ion}} < -1.4$, and $100pc < r < 10kpc$. A rough estimate of the hot wind phase regime is shown in light yellow; this is simply the region where $P_{\text{hot}} > P_{\text{rad}}$, and not informed by models. For comparison, the ratios for the constant density models are shown in blue. *Left panel:* UV diagnostic line ratio diagram with O VI/N V versus O VI/C IV. The radiation-pressure dominated models accurately predict COS spectra of three of the obscured quasars in this diagnostic regime, indicating they are in the radiation-pressure dominated limit. Although J1222+0007’s line ratios fall outside the model-predicted region, its errors suggest it favors the RPC regime. The results of J1255–0339 are inconclusive due to non-detections, but the upper limit observations suggest it may fall within the hot-gas dominated regime. *Right panel:* UV diagnostic line ratio diagram with O VI/[O III] versus O VI/C IV. Two of the objects (J0841+0101 and J1356+1026) fall within the radiation pressure-dominated region, and two more (J1000+1242 and J1222+0007) fall between the radiation pressure and hot wind regimes. Results for J1255–0339 are once again inconclusive due to non-detections. The majority of the objects are closest to the radiation pressure-dominated limit, with one exception.

In Figure 4, we include individual line ratios to compare each object to predictions. The left, top right, and bottom right panels display O VI/[O III], O VI/C IV, and O VI/N V, respectively, plotted against $P_{\text{hot}} < P_{\text{rad}}$.

In all diagnostic plots shown in Figures 3 and 4, J1356+1026 and J0841+0101 fall within the range predicted by radiation pressure-dominated models. The line ratios for J1000+1242 are less consistent but generally align more closely with the radiation pressure-dominated regime, except for O VI/[O III]. For J1222–0007, the uncertainty range includes the hot wind-dominated regime

in the O VI/[O III] vs. O VI/C IV diagnostic plot and the radiation pressure-dominated regime in the O VI/N V vs. O VI/C IV diagnostic plot.

Thus, three out of five targets (J1356+1026, J0841+0101, and J1000+1242) appear consistent with RPC model predictions. This finding echoes results from the pilot study (Somalwar et al. 2020), which also demonstrated that the J1356+1026 line ratios fall near the radiation pressure-dominated limit. The line ratios for J1222–0007 fall around $P_{\text{rad}}/P_{\text{hot}} = 0$, with both the radiation pressure-dominated regime and hot

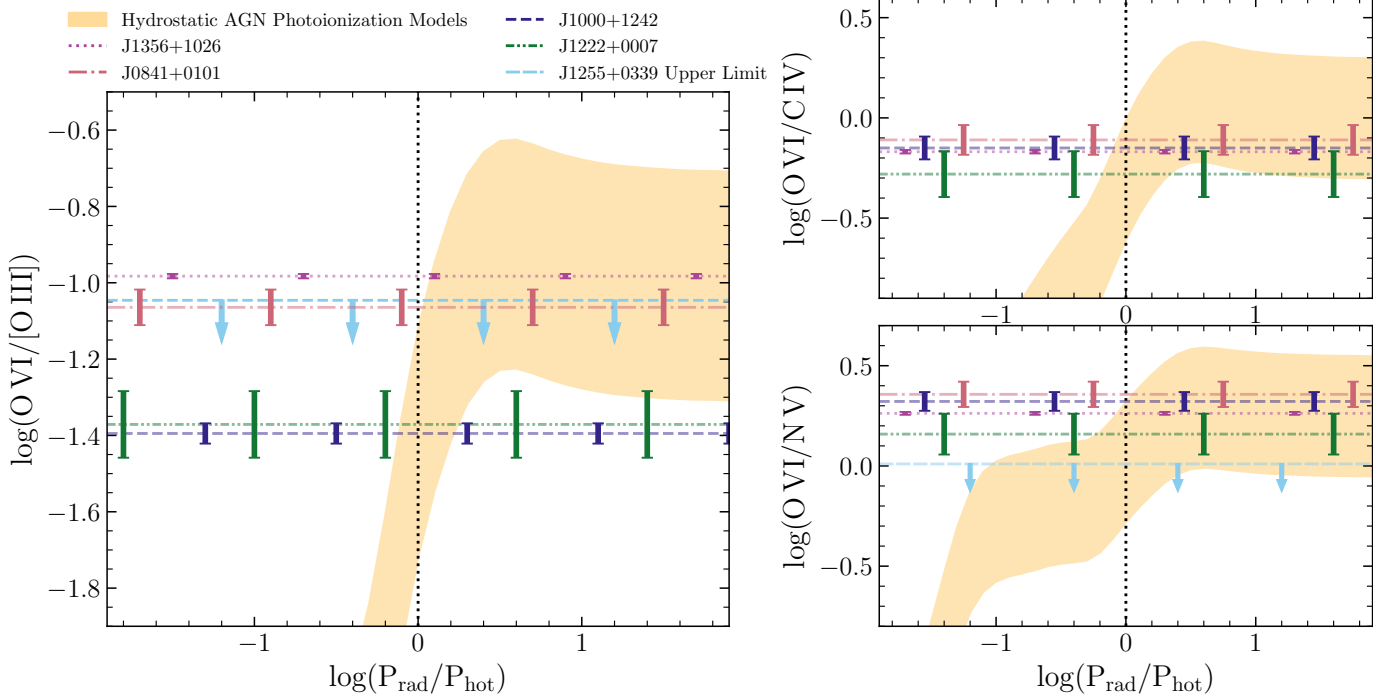


Figure 4: Predicted line ratios versus the relative importance of radiation pressure and hot gas pressure for the theoretical models from (Stern et al. 2016), shown with the UV diagnostic line ratios for the archival sample of five obscured quasars and their respective errors. Each object is plotted with a different color to aid in visual inspection. The legend in the upper left panel applies to all three plots. The J1255–0339 upper-limit O VI and C IV flux estimates are shown with a dashed light blue line and arrows in the left and bottom right diagnostic plots, but omitted from the top right plot since both O VI and C IV are non-detections for this object. In all three plots, a dotted black vertical line indicates the $P_{\text{hot}}/P_{\text{rad}} = 0$ models. Though single line ratios are not as effective diagnostics as the comparative ones in Figure 3, flux measurements intersecting the models to the left of this dotted line suggest hot wind domination, while those to the right indicate radiation pressure domination.

wind-dominated regime within its range of uncertainty. However, the results slightly favor the RPC model, with ratios skewing towards the ($P_{\text{hot}} < P_{\text{rad}}$) range.

J1255+0339 is the least luminous and highest-redshift ($z=0.173$) quasar in our sample and exhibits the weakest UV emission. Concluding what regime the J1255+0339 line ratios fall within is not possible with our results due to the non-detections of C IV and O VI. Upper-limit estimates for these lines are shown in dark blue in Figure 3 and light blue in Figure 4. These estimates suggest the possibility that this object falls within the hot wind-dominated regime, particularly in the case of O VI/N V. Furthermore, the optical diagnostic ratios in the BPT diagram (left panel of Figure 2) show J1255+0339 as the only target in our sample to fall outside the expectations of the radiation pressure-dominated model. Higher-sensitivity measurements without geocoronal Ly α contamination are needed to further diagnose this object.

Though we obtained high-quality measurements of Ly α for each object, we did not include them in our main comparison between the observed UV line ratios

and ionization models due to the significant additional complexity in modeling Ly α emission in the presence of dust and scattering. Nevertheless, we quantify the impact of dust extinction by comparing the Balmer decrement ($H\alpha/H\beta$), a reliable estimate of dust extinction (Domínguez et al. 2013), to the ratio between Ly α and $H\alpha$, as shown in Figure 5. All of our targets exhibit line ratios well below the expected Case B Nebula recombination values, $\text{Ly}\alpha/H\alpha \approx 8.7$ from Hayes (2015) and $H\alpha/H\beta \approx 2.8$ from Jacoby et al. (2001). Furthermore, comparison with the varying $P_{\text{hot}}/P_{\text{rad}}$ model expectations show our targets are consistently dustier than the models.

Notably, all five targets are potential mergers. J1222–0007 has a secondary source ≈ 4.7 arcseconds away (Molyneux et al. 2023). J0841+0101’s dual AGN classification is tentative, and is discussed in (Foord et al. 2020; Comerford et al. 2015; Pfeifle et al. 2023). Sun et al. (2017) suggests that J1255–0339 may be in late stages of a merger based on its morphology and high infrared luminosity. As noted within their appendix, despite its

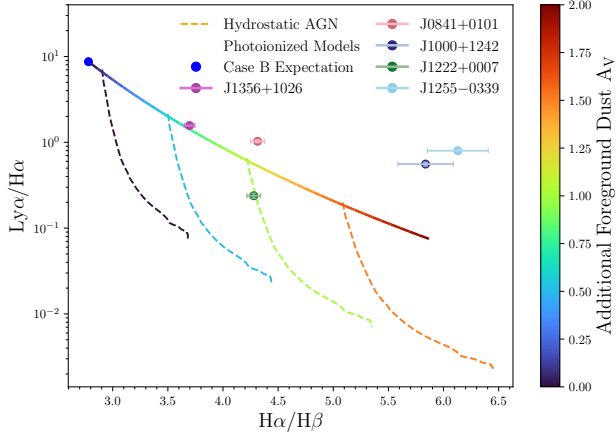


Figure 5: Target Balmer Decrement ($H\alpha/H\beta$) ratios compared to $Ly\alpha/H\alpha$ ratios, shown in comparison to the expected Case B Nebula recombination values, an extinction curve showing how the modified expectation changes for A_v values between 0 and 2, and curves showing the varying P_{rad}/P_{hot} hydrostatic photoionized AGN model expectations attenuated with $A_v=0, 0.5, 1$, and 1.5 . The expected recombination ratios used are $Ly\alpha/H\alpha \approx 8.7$ from Hayes (2015) and $H\alpha/H\beta \approx 2.8$ from Jacoby et al. (2001).

beautiful ≈ 60 kpc spiral features, thought to be tidal tails ionized by the central AGN, it has received little attention in the literature. J1356+1026 is made up of two merging nuclei separated by ≈ 2.5 kpc, as shown by its double-peaked [O III] emission (Dutta & Srianand (2022), Ramos Almeida et al. (2022), Molyneux et al. (2023)). This is consistent with suggestions that luminous Type 2 quasars at low redshift are often triggered by gas funneled to the nucleus during galaxy interactions, as discussed in (Pierce et al. 2023).

6. CONCLUSIONS

This survey examined five radio-quiet, low- z , luminous AGN exhibiting galactic-scale outflows in order to

diagnose the mechanisms driving AGN feedback. By comparing HST COS observations of narrow-line region nuclear emission lines in the FUV range to estimates of P_{rad}/P_{hot} , the ratio of hot gas pressure to radiation pressure predicted by theoretical models, we constrain which driving mechanism dominates the outflows in each case.

Our UV diagnostics suggest that three of our five targets (J1356+1026, J0841+0101, and J1000+1242) align with models predicting radiative-pressure dominated outflows, reflecting the results of a pilot study by Somalwar et al. (2020). Line ratio diagnostics for J1222+0007 slightly favor the radiation pressure-dominated regime, but are inconsistent. The remaining target (J1255+0339) may include a dominant or partial hot wind mechanism, but non-detections of O VI and C IV prevent a robust conclusion.

Comparisons of UV and optical emission line ratios are similarly inconclusive, as they do not appear to fall within the expected model uncertainty.

Although this sample is too small to give conclusive evidence on primary drivers of AGN outflows, it suggests that although the diagnosable targets fall within the radiation pressure-dominated regime, we cannot rule out that both theorized mechanisms could play a role in observed AGN feedback. Further investigations in the UV and optical may further constrain the contribution of a hot wind component and provide conclusions for a broader sample of quasars.

This research is based on observations made with the NASA/ESA Hubble Space Telescope obtained from the Space Telescope Science Institute, which is operated by the Association of Universities for Research in Astronomy, Inc., under NASA contract NAS 5–26555.

These observations are associated with program HST-GO-15935 and funded by grant number HST-GO-15935.021.

REFERENCES

- Abdurro’uf, Accetta, K., Aerts, C., et al. 2022, The Astrophysical Journal Supplement Series, 259, 35, doi: [10.3847/1538-4365/ac4414](https://doi.org/10.3847/1538-4365/ac4414)
- Allen, M. G., Groves, B. A., Dopita, M. A., Sutherland, R. S., & Kewley, L. J. 2008, The Astrophysical Journal Supplement Series, 178, 20, doi: [10.1086/589652](https://doi.org/10.1086/589652)
- Allington-Smith, J., Breare, M., Ellis, R., et al. 1994, Publications of the Astronomical Society of the Pacific, 106, 983, doi: [10.1086/133471](https://doi.org/10.1086/133471)
- Arakawa, N., Fabian, A. C., Ferland, G. J., & Ishibashi, W. 2022, Monthly Notices of the Royal Astronomical Society, 517, 5069, doi: [10.1093/mnras/stac3044](https://doi.org/10.1093/mnras/stac3044)
- Barbary, K. 2021, extinction: Dust extinction laws, Astrophysics Source Code Library, record ascl:2102.026
- Baskin, A., Laor, A., & Stern, J. 2013, Monthly Notices of the Royal Astronomical Society, 438, 604, doi: [10.1093/mnras/stt2230](https://doi.org/10.1093/mnras/stt2230)

- . 2014, *Monthly Notices of the Royal Astronomical Society*, 445, 3025, doi: [10.1093/mnras/stu1732](https://doi.org/10.1093/mnras/stu1732)
- Behroozi, P. S., Wechsler, R. H., & Conroy, C. 2013, *ApJ*, 770, 57, doi: [10.1088/0004-637X/770/1/57](https://doi.org/10.1088/0004-637X/770/1/57)
- Bessiere, P. S., Almeida, C. R., Holden, L. R., Tadhunter, C. N., & Canalizo, G. 2024, QSOFEED: The relationship between star formation and AGN Feedback. <https://arxiv.org/abs/2405.06421>
- Bianchi, S., Guainazzi, M., Laor, A., Stern, J., & Behar, E. 2019, *Monthly Notices of the Royal Astronomical Society*, 485, 416, doi: [10.1093/mnras/stz430](https://doi.org/10.1093/mnras/stz430)
- Bower, R. G., Benson, A. J., Malbon, R., et al. 2006, *MNRAS*, 370, 645, doi: [10.1111/j.1365-2966.2006.10519.x](https://doi.org/10.1111/j.1365-2966.2006.10519.x)
- Brinchmann, J., Charlot, S., White, S. D. M., et al. 2004, *MNRAS*, 351, 1151, doi: [10.1111/j.1365-2966.2004.07881.x](https://doi.org/10.1111/j.1365-2966.2004.07881.x)
- Cattaneo, A., Faber, S. M., Binney, J., et al. 2009, *Nature*, 460, 213, doi: [10.1038/nature08135](https://doi.org/10.1038/nature08135)
- Comerford, J. M., Pooley, D., Barrows, R. S., et al. 2015, Merger-driven Fueling of Active Galactic Nuclei: Six Dual and Offset Active Galactic Nuclei Discovered with Chandra and Hubble Space Telescope Observations. <https://arxiv.org/abs/1504.01391>
- Domínguez, A., Siana, B., Henry, A. L., et al. 2013, *The Astrophysical Journal*, 763, 145, doi: [10.1088/0004-637x/763/2/145](https://doi.org/10.1088/0004-637x/763/2/145)
- Dopita, M. A., Groves, B. A., Sutherland, R. S., Binette, L., & Cecil, G. 2002, *The Astrophysical Journal*, 572, 753, doi: [10.1086/340429](https://doi.org/10.1086/340429)
- Draine, B. T. 2011, *Physics of the Interstellar and Intergalactic Medium*
- Dutta, R., & Srianand, R. 2022, *Monthly Notices of the Royal Astronomical Society*, 516, 4338–4345, doi: [10.1093/mnras/stac2483](https://doi.org/10.1093/mnras/stac2483)
- Faucher-Giguère, C.-A., & Quataert, E. 2012, *Monthly Notices of the Royal Astronomical Society*, 425, 605–622, doi: [10.1111/j.1365-2966.2012.21512.x](https://doi.org/10.1111/j.1365-2966.2012.21512.x)
- Ferland, G. J., Chatzikos, M., Guzmán, F., et al. 2017, *RMxAA*, 53, 385, doi: [10.48550/arXiv.1705.10877](https://doi.org/10.48550/arXiv.1705.10877)
- Fitzpatrick, E. L. 1999, *PASP*, 111, 63, doi: [10.1086/316293](https://doi.org/10.1086/316293)
- Foord, A., Gültekin, K., Nevin, R., et al. 2020, *The Astrophysical Journal*, 892, 29, doi: [10.3847/1538-4357/ab72fa](https://doi.org/10.3847/1538-4357/ab72fa)
- Foreman-Mackey, D., Hogg, D. W., Lang, D., & Goodman, J. 2013, *PASP*, 125, 306, doi: [10.1086/670067](https://doi.org/10.1086/670067)
- Green, J. C., Froning, C. S., Osterman, S., et al. 2012, *ApJ*, 744, 60, doi: [10.1088/0004-637X/744/1/60](https://doi.org/10.1088/0004-637X/744/1/60)
- Greene, J. E., Zakamska, N. L., Ho, L. C., & Barth, A. J. 2011, *ApJ*, 732, 9, doi: [10.1088/0004-637X/732/1/9](https://doi.org/10.1088/0004-637X/732/1/9)
- Greene, J. E., Zakamska, N. L., & Smith, P. S. 2012, *ApJ*, 746, 86, doi: [10.1088/0004-637X/746/1/86](https://doi.org/10.1088/0004-637X/746/1/86)
- Groves, B. A., Dopita, M. A., & Sutherland, R. S. 2004, *The Astrophysical Journal Supplement Series*, 153, 9–73, doi: [10.1086/421113](https://doi.org/10.1086/421113)
- Groves, B. A., Heckman, T. M., & Kauffmann, G. 2006, *Monthly Notices of the Royal Astronomical Society*, 371, 1559, doi: [10.1111/j.1365-2966.2006.10812.x](https://doi.org/10.1111/j.1365-2966.2006.10812.x)
- Hardcastle, M., & Croston, J. 2020, *New Astronomy Reviews*, 88, 101539, doi: <https://doi.org/10.1016/j.newar.2020.101539>
- Harrison, C. M. 2017, *Nature Astronomy*, 1, 0165, doi: [10.1038/s41550-017-0165](https://doi.org/10.1038/s41550-017-0165)
- Harrison, C. M., Alexander, D. M., Mullaney, J. R., & Swinbank, A. M. 2014, *MNRAS*, 441, 3306, doi: [10.1093/mnras/stu515](https://doi.org/10.1093/mnras/stu515)
- Hayes, M. 2015, *Publications of the Astronomical Society of Australia*, 32, doi: [10.1017/pasa.2015.25](https://doi.org/10.1017/pasa.2015.25)
- Ishibashi, W., Fabian, A. C., & Maiolino, R. 2018, *Monthly Notices of the Royal Astronomical Society*, doi: [10.1093/mnras/sty236](https://doi.org/10.1093/mnras/sty236)
- Jacoby, G. H., Ferland, G. J., & Korista, K. T. 2001, *ApJ*, 560, 272, doi: [10.1086/322489](https://doi.org/10.1086/322489)
- Kaiser, M. E., Hodge, P. E., Keyes, C., et al. 2008, in *Society of Photo-Optical Instrumentation Engineers (SPIE) Conference Series*, Vol. 7014, *Ground-based and Airborne Instrumentation for Astronomy II*, ed. I. S. McLean & M. M. Casali, 70146G, doi: [10.1117/12.790239](https://doi.org/10.1117/12.790239)
- Kauffmann, G., Heckman, T. M., Tremonti, C., et al. 2003, *Monthly Notices of the Royal Astronomical Society*, 346, 1055–1077, doi: [10.1111/j.1365-2966.2003.07154.x](https://doi.org/10.1111/j.1365-2966.2003.07154.x)
- Kewley, L. J., Groves, B., Kauffmann, G., & Heckman, T. 2006, *MNRAS*, 372, 961, doi: [10.1111/j.1365-2966.2006.10859.x](https://doi.org/10.1111/j.1365-2966.2006.10859.x)
- King, A. R., Zubovas, K., & Power, C. 2011, *Monthly Notices of the Royal Astronomical Society: Letters*, 415, L6–L10, doi: [10.1111/j.1745-3933.2011.01067.x](https://doi.org/10.1111/j.1745-3933.2011.01067.x)
- Kormendy, J., & Ho, L. C. 2013, *ARA&A*, 51, 511, doi: [10.1146/annurev-astro-082708-101811](https://doi.org/10.1146/annurev-astro-082708-101811)
- Laha, S., Reynolds, C. S., Reeves, J., et al. 2021, *Nature Astronomy*, 5, 13, doi: [10.1038/s41550-020-01255-2](https://doi.org/10.1038/s41550-020-01255-2)
- Laor, A., & Draine, B. T. 1993, *ApJ*, 402, 441, doi: [10.1086/172149](https://doi.org/10.1086/172149)
- Leung, G. C. K., Coil, A. L., Aird, J., et al. 2019, *ApJ*, 886, 11, doi: [10.3847/1538-4357/ab4a7c](https://doi.org/10.3847/1538-4357/ab4a7c)
- Martín-Navarro, I., Brodie, J. P., Romanowsky, A. J., Ruiz-Lara, T., & van de Ven, G. 2018, *Nature*, 553, 307, doi: [10.1038/nature24999](https://doi.org/10.1038/nature24999)
- Mathis, J. S., Rumpl, W., & Nordsieck, K. H. 1977, *ApJ*, 217, 425, doi: [10.1086/155591](https://doi.org/10.1086/155591)
- Meena, B., Crenshaw, D. M., Schmitt, H. R., et al. 2021, *ApJ*, 916, 31, doi: [10.3847/1538-4357/ac0246](https://doi.org/10.3847/1538-4357/ac0246)

- Molyneux, S. J., Rivera, G. C., Breuck, C. D., et al. 2023, The Quasar Feedback Survey: characterising CO excitation in quasar host galaxies. <https://arxiv.org/abs/2310.10235>
- Morganti, R. 2017, *Frontiers in Astronomy and Space Sciences*, 4, 42, doi: [10.3389/fspas.2017.00042](https://doi.org/10.3389/fspas.2017.00042)
- Mullaney, J. R., Alexander, D. M., Fine, S., et al. 2013, *Monthly Notices of the Royal Astronomical Society*, 433, 622–638, doi: [10.1093/mnras/stt751](https://doi.org/10.1093/mnras/stt751)
- Murray, N., Quataert, E., & Thompson, T. A. 2005, *The Astrophysical Journal*, 618, 569–585, doi: [10.1086/426067](https://doi.org/10.1086/426067)
- Namekata, D., Umemura, M., & Hasegawa, K. 2014, *Monthly Notices of the Royal Astronomical Society*, 443, 2018–2048, doi: [10.1093/mnras/stu1271](https://doi.org/10.1093/mnras/stu1271)
- Netzer, H. 2021, *Monthly Notices of the Royal Astronomical Society*, 509, 2637, doi: [10.1093/mnras/stab3133](https://doi.org/10.1093/mnras/stab3133)
- Newville, M., Stensitzki, T., Allen, D. B., & Ingargiola, A. 2015, LMFIT: Non-Linear Least-Square Minimization and Curve-Fitting for Python, 0.8.0, Zenodo, doi: [10.5281/zenodo.11813](https://doi.org/10.5281/zenodo.11813)
- Osterbrock, D. E., & Ferland, G. J. 2006, *Astrophysics of gaseous nebulae and active galactic nuclei*
- Pfeifle, R. W., Weaver, K., Satyapal, S., et al. 2023, *NuSTAR Observations of Four Mid-IR Selected Dual AGN Candidates in Galaxy Mergers*. <https://arxiv.org/abs/2306.16437>
- Pierce, J. C. S., Tadhunter, C., Ramos Almeida, C., et al. 2023, *Monthly Notices of the Royal Astronomical Society*, 522, 1736–1751, doi: [10.1093/mnras/stad455](https://doi.org/10.1093/mnras/stad455)
- Polednikova, J., Ederoclite, A., Cepa, J., et al. 2015, *AA*, 578, A121, doi: [10.1051/0004-6361/201525952](https://doi.org/10.1051/0004-6361/201525952)
- Ramos Almeida, C., Bischetti, M., García-Burillo, S., et al. 2022, *Astronomy and Astrophysics*, 658, A155, doi: [10.1051/0004-6361/202141906](https://doi.org/10.1051/0004-6361/202141906)
- Reyes, R., Zakamska, N. L., Strauss, M. A., et al. 2008, *The Astronomical Journal*, 136, 2373–2390, doi: [10.1088/0004-6256/136/6/2373](https://doi.org/10.1088/0004-6256/136/6/2373)
- Richings, A. J., Faucher-Giguère, C.-A., & Stern, J. 2021, *Monthly Notices of the Royal Astronomical Society*, 503, 1568, doi: [10.1093/mnras/stab556](https://doi.org/10.1093/mnras/stab556)
- Salim, S., Rich, R. M., Charlot, S., et al. 2007, *The Astrophysical Journal Supplement Series*, 173, 267–292, doi: [10.1086/519218](https://doi.org/10.1086/519218)
- Schlafly, E. F., & Finkbeiner, D. P. 2011, *ApJ*, 737, 103, doi: [10.1088/0004-637X/737/2/103](https://doi.org/10.1088/0004-637X/737/2/103)
- Singha, M., O’Dea, C. P., & Baum, S. A. 2023, *Galaxies*, 11, doi: [10.3390/galaxies11040085](https://doi.org/10.3390/galaxies11040085)
- Soderblom, D., et al. 2022, *COS Data Handbook*, 5th edn., Space Telescope Science Institute, Baltimore
- Somalwar, J., Johnson, S. D., Stern, J., et al. 2020, *ApJL*, 890, L28, doi: [10.3847/2041-8213/ab733d](https://doi.org/10.3847/2041-8213/ab733d)
- Stern, J., Behar, E., Laor, A., Baskin, A., & Holczer, T. 2014, *Monthly Notices of the Royal Astronomical Society*, 445, 3011–3024, doi: [10.1093/mnras/stu1960](https://doi.org/10.1093/mnras/stu1960)
- Stern, J., Faucher-Giguère, C.-A., Zakamska, N. L., & Hennawi, J. F. 2016, *The Astrophysical Journal*, 819, 130, doi: [10.3847/0004-637x/819/2/130](https://doi.org/10.3847/0004-637x/819/2/130)
- Stern, J., Laor, A., & Baskin, A. 2013, *Monthly Notices of the Royal Astronomical Society*, 438, 901–921, doi: [10.1093/mnras/stt1843](https://doi.org/10.1093/mnras/stt1843)
- Su, K.-Y., Hopkins, P. F., Bryan, G. L., et al. 2021, *Monthly Notices of the Royal Astronomical Society*, 507, 175, doi: [10.1093/mnras/stab2021](https://doi.org/10.1093/mnras/stab2021)
- Sun, A.-L., Greene, J. E., & Zakamska, N. L. 2017, *ApJ*, 835, 222, doi: [10.3847/1538-4357/835/2/222](https://doi.org/10.3847/1538-4357/835/2/222)
- Tremonti, C. A., Heckman, T. M., Kauffmann, G., et al. 2004, *ApJ*, 613, 898, doi: [10.1086/423264](https://doi.org/10.1086/423264)
- Weigel, A. K., Schawinski, K., Caplar, N., et al. 2017, *ApJ*, 845, 134, doi: [10.3847/1538-4357/aa803b](https://doi.org/10.3847/1538-4357/aa803b)
- York, D. G., Adelman, J., Anderson, John E., J., et al. 2000, *AJ*, 120, 1579, doi: [10.1086/301513](https://doi.org/10.1086/301513)
- Zakamska, N. L., & Greene, J. E. 2014, *MNRAS*, 442, 784, doi: [10.1093/mnras/stu842](https://doi.org/10.1093/mnras/stu842)
- Zubovas, K., & King, A. 2012, *AGN Winds and the Black-Hole - Galaxy Connection*. <https://arxiv.org/abs/1201.3540>